The Monte Carlo Method: Versatility Unbounded in a Dynamic Computing World
Chattanooga, Tennessee, April 17-21, 2005, on CD-ROM, American Nuclear Society, LaGrange Park, IL (2005)

A GENERALIZED BOLTZMANN FOKKER-PLANCK ELECTRON TRANSPORT METHOD

Brian C. Franke
Sandia National Laboratories
P.O. Box 5800, MS 1179, Albuquerque, NM 87185
bcfrank@sandia.gov

Anil K. Prinja
Chemical and Nuclear Engineering Department
University of New Mexico
209 Farris Engineering Center, Albuquerque, NM 87131
prinja@unm.edu

ABSTRACT

We present a transport-based method for electrons that incorporates the correct transport mechanics and is computationally efficient for implementation in single event Monte Carlo codes. The method yields accurate dose profiles, as well as angular and energy distributions, across a broad range of energies in heterogeneous media, and presents a viable alternative to the established condensed history method. Our approach is mathematically rigorous, building on higher order Fokker-Planck and Boltzmann Fokker-Planck representations of the scattering process, and we accordingly refer to it as a Generalized Boltzmann Fokker-Planck (GBFP) approach.

We postulate the existence of single collision scattering distributions (differential cross sections) and impose the constraint that the first few momentum transfer moments be identical to corresponding analog values. The form of the approximate scattering kernel is not strictly constrained, and we have implemented several reasonable choices. This procedure yields a transport model characterized by longer mean free paths and smoother scattering kernels. In practice, acceptable accuracy is achieved with two rigorously preserved moments, but accuracy can be systematically increased to analog level by preserving successively higher moments with almost no change to the algorithm. Details of specific moment-preserving strategies are described. Results are presented for dose in heterogeneous media due to a pencil beam and a line source of monoenergetic electrons. Error and runtimes of our GBFP formulations are contrasted against two different condensed history implementations.

Key Words: Monte Carlo, electron transport, Boltzmann Fokker-Planck

1 INTRODUCTION

The condensed history method [1] has long been used for electron transport calculations, and the theoretical basis of the method has been extensively evaluated in recent times [2, 3]. Condensed history has proven to be an effective approach for modeling realistic transport problems. However, it is known to have some deficiencies, such as inaccuracy near material boundaries and indistinguishability of pathlength and displacement. Several "fixes" have been implemented, some more systematic than others, but the fact remains that the alogrithm is often fundamentally altered in order to circumvent the inherent shortcomings. In recent years several

methods have been proposed as alternatives to the condensed history technique [4, 5, 6, 7]. A common feature of these methods is that an approximate transport problem is solved, characterized by a longer mean free path and a smoother or less forward peaked differential cross section than analog values. These approximate schemes differ in the strategies employed to construct model cross sections but a hallmark of all approaches is that accuracy can be systematically increased by retaining increasingly more accurate physics; indeed several of these methods limit to analog accuracy. Moreover, the correct transport mechanics is naturally accomodated with the use of an explicitly linear transport (Markovian) formulation as the physical and mathematical basis of the approach. In particular, with Poisson collision statistics, the new algorithms handle material and vacuum interfaces naturally. That is, no alteration of the tracking algorithm is necessary for boundary crossings. All these features combine to make computationally efficient single event Monte Carlo simulation feasible for charged particles in general and electron transport in particular.

Theoretical analysis shows that sensitivity of the transport process to elastic scattering is well captured by angular moments of the underlying DCS, specifically the generalized momentum transfer moments. It is well known, for instance, that if scattering is sufficiently forward peaked the Boltzmann scattering operator can be approximated by the angular diffusion or Fokker-Planck (FP) operator with the diffusion coefficient given by the transport cross section, which is just the first momentum transfer moment. Moreover, it has been shown that large scattering-angle effects can be incorporated using higher order Fokker Planck expansions and this essentially amounts to an expansion in higher order momentum transfer moments. However, truncated higher order FP expansions are not mathematically stable and the challenge is to construct equivalent Boltzmann collision operators that possess the same generalized FP expansion up to a finite order as the analog case. This can be achieved in practice by preserving an appropriate number of momentum transfer moments in conjunction with a strategy to construct a suitable scattering kernel. Here we demonstrate a number of such strategies which prove computationally efficient and accurate for energetic electron transport. Our approach builds on higher order Fokker-Planck and Boltzmann Fokker-Planck representations of the scattering process, and we accordingly refer to it as a Generalized Boltzmann Fokker-Planck (GBFP) approach.

Various strategies are presented in the next section and their numerical implementation for a heterogeneous medium demonstrated in Section 3. Numerical results are discussed in Section 4 where the accuracy of the methods is assessed using analog benchmark calculations. This is followed by a comparison of computational efficiencies with condensed history methods in Section 5. We do not consider inelastic scattering in this paper and use the continuous slowing down (CSD) approximation to simplify the comparison of our GBFP and condensed history angular scattering algorithms. The GBFP approach to inelastic scattering has been considered elsewhere [8, 9] and is independent of the elastic scattering approximation. We conclude in Section 6 with a few final observations.

2 ANGULAR SCATTERING MODELS

The angular flux $\Psi(\vec{r}, E, \vec{\Omega})$ of electrons at spatial location $\vec{r}(x, y, z)$ traveling in direction $\vec{\Omega}(\mu, \phi)$ with energy E satisfies the following transport equation,

$$\vec{\Omega} \cdot \nabla\Psi - \frac{\partial}{\partial E}\left[S(\vec{r}, E)\,\Psi\right] + \sigma_s(\vec{r}, E)\,\Psi = \int_{4\pi} \sigma_s(\vec{r}, \vec{\Omega} \cdot \vec{\Omega}', E)\,\Psi(\vec{r}, \vec{\Omega}', E) d\vec{\Omega}', \tag{1}$$

where $\sigma_s(\vec{r}, E)$ is the total electron scattering cross section, $\sigma_s(\vec{r}, \vec{\Omega} \cdot \vec{\Omega}', E)$ is the differential scattering cross section and $S(\vec{r}, E)$ the material stopping power. The true differential cross section (DCS) for electron scattering is highly peaked about $\vec{\Omega} \cdot \vec{\Omega}' \equiv \mu_0 = 1$ while the corresponding total scattering cross section is large. As a consequence, this analog problem is computationally very expensive when implemented in single event Monte Carlo.

We define momentum transfer moments of the elastic DCS as

$$\sigma_n(\vec{r}, E) \equiv 2\pi \int_{-1}^{1} d\mu_0\,(1 - \mu_0)^n \sigma_s(\vec{r}, \mu_0, E), \quad n = 1, 2, \ldots \tag{2}$$

Note that σ_1 is just the familiar transport cross section and all moments σ_n are positive for a positive DCS. Moreover, for a sufficiently peaked DCS, they form a rapidly decreasing sequence which indicates that the important physics of elastic scattering interactions can be captured by the first few moments. This observation is key to the efficiency and accuracy of our approach.

The essence of our method is to replace $\sigma_s(\vec{r}, \mu_0, E)$ by an approximate DCS, $\tilde{\sigma}_s(\vec{r}, \mu_0, E)$, such that the associated momentum transfer moments $\tilde{\sigma}_n$ are identical to the exact moments σ_n for $n = 1, 2 \ldots N$, where N is arbitrary but finite. All higher moments, as well as σ_0, are approximated in terms of these N moments. By not rigorously preserving all momentum transfer moments we are modeling a scattering process with a longer mean free path (mfp) than the actual mfp and a less peaked angular-scattering distribution. On the other hand, *strictly* preserving a number of low-order moments should ensure some measure of accuracy. This approach is motivated in part by Lewis theory [10], which demonstrates a direct correlation between preserving moments of the DCS and the accuracy of the model as measured by space-angle moments of the infinite medium solution, and in part by the effectiveness of moment-preservation in Generalized Fokker-Planck expansions [5, 6, 7].

We have implemented this method with several forms of the approximate DCS: purely discrete scattering angles [11], a discrete scattering angle hybridized with a smooth screened Rutherford kernel [12], and an exponential scattering distribution hybridized with a smooth screened Rutherford kernel [13]. We briefly describe each of these scattering kernels in the following subsections.

2.1 Discrete

Perhaps the simplest approach, conceptually and from practical point of view, is to represent $\tilde{\sigma}_s$ as a superposition of discrete scattering angles, as follows:

$$\tilde{\sigma}_s(\vec{r}, \mu_0, E) = \sum_{n=1}^{N} \frac{\alpha_n(\vec{r}, E)}{2\pi}\,\delta\left[\mu_0 - \xi_n(\vec{r}, E)\right]. \tag{3}$$

The scattering amplitudes $\{\alpha_n,\, n = 1, 2 \ldots\ N\}$ and scattering cosines $\{\xi_n,\, n = 1, 2 \ldots\ N\}$ are then constrained to yield the exact first $2N$ momentum transfer moments $\{\tilde{\sigma}_n = \sigma_n,\, n = 1, 2 \ldots 2N\}$ as given by Eq. (2). This condition yields a nonlinear algebraic system for the α_n and ξ_n that can be solved using a robust algorithm by Sloan [14]. Discrete angle representations were first introduced in neutral particle transport in the MORSE code [15] and the idea was subsequently extended by Sloan [14] and Morel [16] for peaked scattering. This approach or strategy, while easy to implement and potentially very accurate, displays ray-effects in transmitted and reflected angular distributions when few discrete angles are used and when the material is optically thin. The next two subsections describe ways to mitigate or eliminate ray-effects without affecting the moment-preserving feature of this approach.

2.2 Hybrid Discrete

Ray-effect mitigation in the discrete scattering-angle formalism can be realized by the superposition of a continuous in angle, or smooth, component that has a long associated mean free path, is not forward peaked, and is easy to sample from. Furthermore, by requiring the large scattering angle shape and amplitude of this smooth component to be identical or close to the corresponding analog cross section, the higher angular moments will be accurately, if not exactly, captured. For the screened Rutherford DCS this decomposition into discrete and smooth components can be effected as follows:

$$\tilde{\sigma}_s(\vec{r}, \mu_0, E) = \frac{\sigma_0(\vec{r}, E)}{2\pi} \frac{2\eta^*(\vec{r}, E)\,(1 + \eta^*(\vec{r}, E))}{(1 + 2\eta^*(\vec{r}, E) - \mu_0)^2} + \sum_{l=1}^{L} \frac{\alpha_l(\vec{r}, E)}{2\pi}\, \delta\left[\mu_0 - \xi_l(\vec{r}, E)\right]. \qquad (4)$$

The first term is just the screened Rutherford scattering kernel [17] but with η^* chosen to yield a long mfp and hence a smooth angular distribution. The second term is the discrete scattering-angle model discussed in Section 2.1. The choice of η^* is somewhat arbitrary, providing that it is larger than the analog value. A larger value of η^* produces a greater speed-up but is more approximate. The strategy we have adopted is to select this parameter to give a smooth component mean free path that is related to the step size in condensed history methods. Once η^* is thus chosen, the discrete scattering cosines and amplitudes are calculated by preserving the residual cross section moments. Numerical testing has shown ray-effects with just one discrete component are greatly reduced or become practically indiscernible with the addition of a continuous component.

2.3 Hybrid Exponential

Ray-effects can be eliminated altogether by employing a completely continuous scattering kernel that preserves enough angular moments of the DCS. We have shown using a Generalized Fermi expansion [13] that a kernel based on exponentials can rigorously preserve angular moments while remaining robust. Our specific numerical implementation has included a single exponential, which exactly preserves the first two momentum transfer moments, and an exponential kernel hybridized with the smoothed Rutherford part to capture both forward-peaked and large-angle scattering components. The latter decomposition can be expressed as:

$$\tilde{\sigma}_s(\vec{r}, \mu_0, E) = \frac{\sigma_0(\vec{r}, E)}{2\pi} \frac{2\eta^*(\vec{r}, E)\,(1 + \eta^*(\vec{r}, E))}{(1 + 2\eta^*(\vec{r}, E) - \mu_0)^2} + \frac{A(\vec{r}, E)}{2\beta(\vec{r}, E)} \exp\left[-\frac{(1 - \mu_0)}{2\beta(\vec{r}, E)}\right], \qquad (5)$$

As with the hybrid discrete kernel, η^* is chosen to yield an appropriately long mfp and a smooth angular distribution. The parameters A and β are calculated from the residual cross section moments.

3 COMPUTATIONAL METHODS

The computational results presented here are obtained with restricted physics both for simplicity of implementation and to isolate the effects of the angular scattering algorithms being tested. Thus, no secondary photons or electrons are simulated, a continuous-slowing-down (CSD) approximation is used in all calculations and analog angular scattering is modeled using the screened Rutherford scattering model [17]. The energy dependence of the simulation is accomplished by defining physical parameters on an energy grid. These parameters are generated by the XGEN cross section generating code [20].

The method we label as "ITS-like" condensed history applies the multiple-scattering angular deflection of the particle at the end of each step, i.e. the end of the pathlength for which the angular deflection has been precomputed. The algorithm differs from the implementation in the ITS codes in that: our angular distribution is based only on screened Rutherford scattering and ignores inelastic scattering angular deflection; we sample from the precomputed angular deflection distribution nearest in energy to the particle energy when the angular deflection is applied; and we have implemented a simpler (and less accurate) material boundary crossing algorithm. These modifications simplify the implementation and provide a consistent basis for comparison with the analog calculations and GBFP methods. The same simplifications apply to the "Random Hinge" condensed history algorithm. It differs from the ITS-like algorithm only in that the angular deflection of the particle is applied at a uniformly sampled random position within each step.

There are many intricate algorithms that have been proposed to cope with the boundary crossing problem in condensed history methods (see Ref. [21] for example). We have implemented an admittedly simple boundary crossing algorithm. When a material interface is encountered, the step-size (in condensed history) or the sampled distance-to-collision (in GBFP or analog transport) is scaled by the ratio of the total cross sections in the two materials, such that the distance is preserved as measured in mean free paths.

The runtime comparisons presented here should be considered approximate. Undoubtedly, some algorithmic improvements could be made to accelerate each of the implementations and runtime variations would be experienced with different compilers or computer architectures. For detailed dose results, particles were tracked through a Cartesian tally grid, and this tracking was the dominant fraction of runtime for the faster calculations. Therefore, the runtimes presented are for calculations that omit the detailed tally grid. Instead runtimes are based on identical calculations with minimal geometry boundaries for defining the problem.

4 RESULTS

To test the methods described in this paper and to compare their efficiencies against condensed history methods, two problems have been simulated, one with a line source of

electrons incident on a heterogenous block of water (simulating tissue) containing bone, and the other with pencil beam incidence on the same geometry. Fig. 1 illustrates this geometry, with Fig. 1(a) showing the line source and Fig. 1(b) showing the pencil beam source. Both sources are 10 MeV monoenergetic and normally incident on the block of water. The pencil beam is slightly offset from the material boundary at the middle of the block to avoid numerical difficulties.

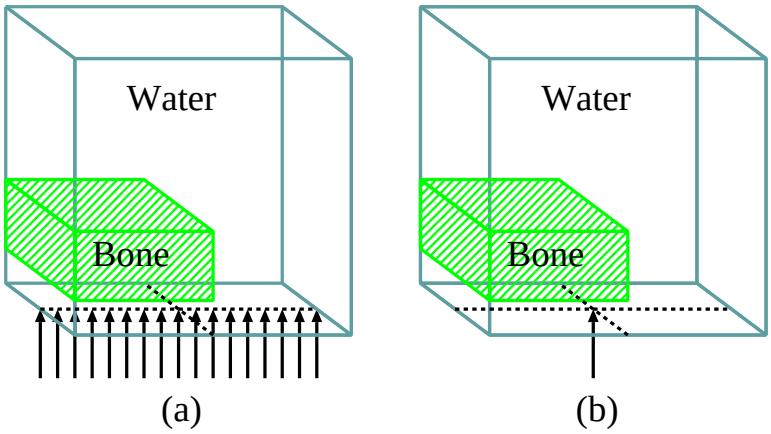

Figure 1: The problem geometry with (a) the line source and (b) the pencil beam source.

The dose distributions for the two problems were calculated with each of the approximate scattering kernels and with the analog scattering kernel. The dose was integrated through the block in the same direction that the bone slab passes through. The dose for the line source analog calculation is shown in Fig. 2. The energy deposition in these plots is shown in keV per gram per source electron. (The normalization by density accounts for the lowered values in the bone region of the line source problem.)

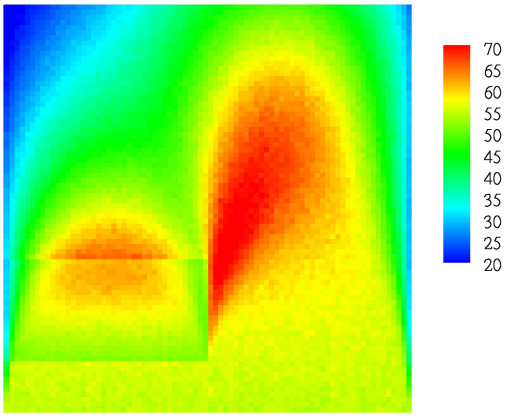

Figure 2: The analog dose deposition in keV/g in the problem geometry with a monodirectional line source.

A suite of calculations was performed with each of the approximate scattering kernels by varying the parameter that affects the speed of the kernel. For each of these approximate calculations, the distribution of the error in the dose was calculated relative to the analog calculation. Since numerous calculations were performed with varying parameters in the scattering kernels, only a few illustrative results can be shown. For calculation runtimes of approximately 30 minutes, errors are shown in Fig. 3.

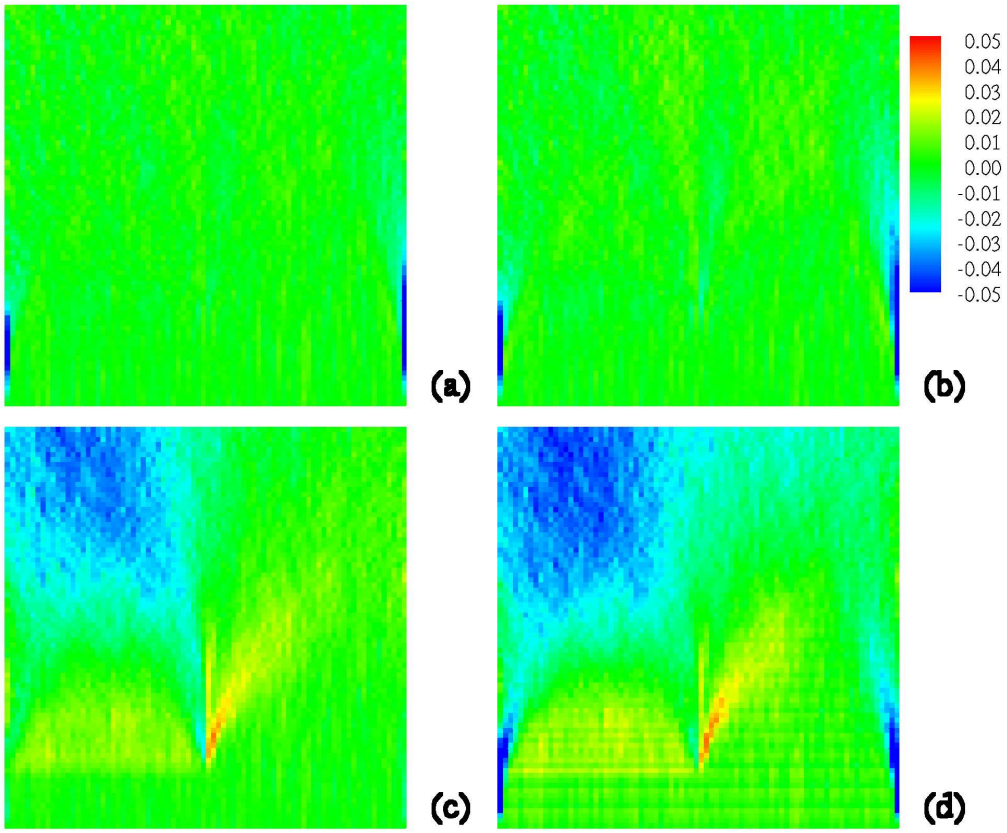

Figure 3: The relative error fraction in dose deposition with a monodirectional line source. For similar runtimes, errors are shown for (a) hybrid discrete, (b) hybrid exponential, (c) random hinge, and (d) ITS-like condensed history.

The important sources of error can be discerned from these plots. In Figs. 3(c) and 3(d) the condensed history errors are mostly due to errors in the material boundary crossings. Especially in the case of the random hinge, the regions of signifi cant error can be attributed to electrons crossing the bone-water interface. In Figs. 3(a), 3(b), and 3(d) there are signifi cant errors at both sides of the block near the bottom. These errors (overestimation of the dose by the approximate method) are due to overestimation of the uncollided flux. The methods do not allow the proper amount of radiation to escape from the side of the block. (Random hinge results using longer steps show similar errors.)

Similarly, an analog simulation was performed with the pencil beam source, and the resulting dose distribution is shown in Fig. 4. A suite of calculations was performed with the approximate

scattering methods. For runtimes of approximately 30 minutes, errors are shown in Fig. 5.

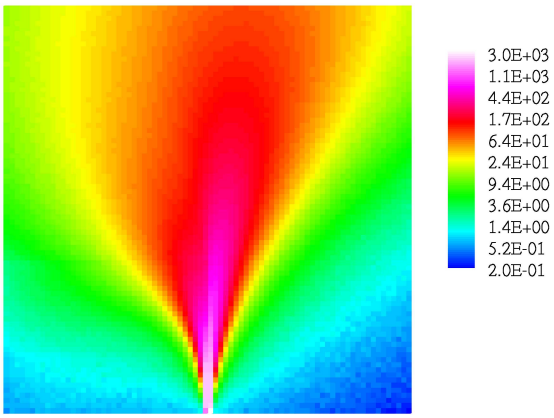

Figure 4: The analog dose deposition in keV/g in the problem geometry with a pencil beam source.

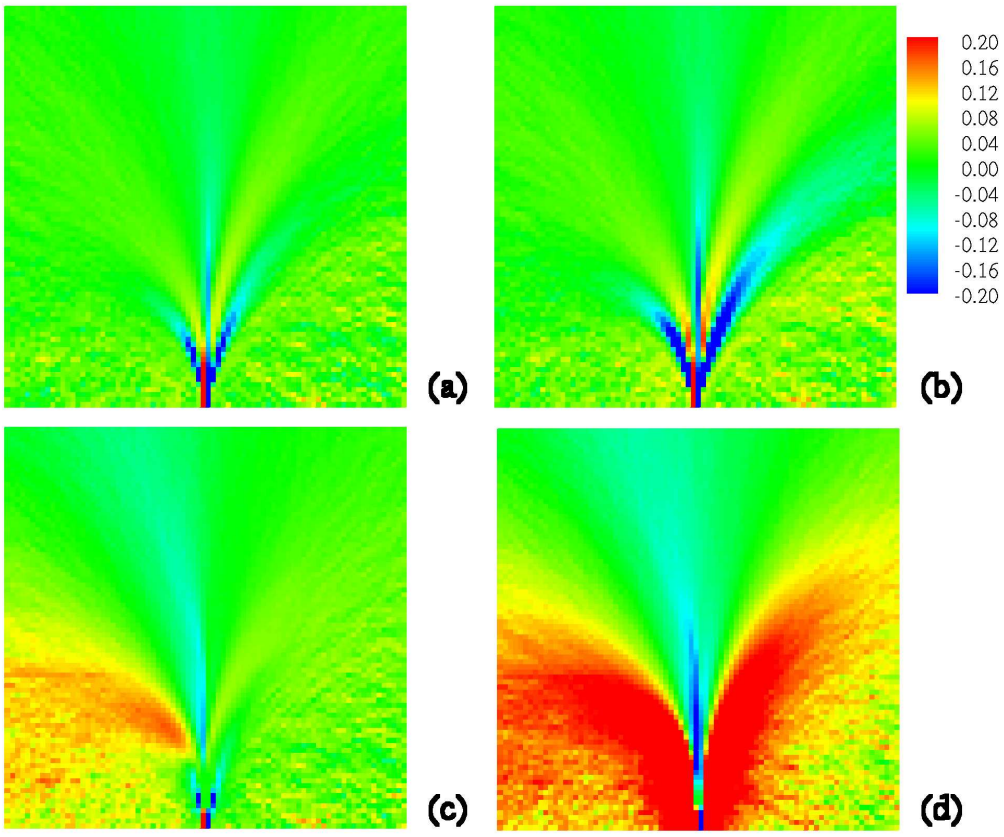

Figure 5: The relative error fraction in dose deposition with a pencil beam source. For similar runtimes, errors are shown for (a) hybrid discrete, (b) hybrid exponential, (c) random hinge, and (d) ITS-like condensed history.

In Fig. 5 the sources of error appear differently from those in the line source results. At the bottom edge of the slab where the beam is incident, there is a line of dose overestimation (blue) extending into the slab to the right of a line of dose underestimation (red) in all four plots. This is because the normally-incident source is slightly to the right of the boundary between these tally cells. This exaggerates beyond the resolution of the tally structure the problem of overestimating uncollided flux in the approximate methods (i.e., not allowing sufficient particles to scatter into the adjacent tally cell). The GBFP kernels in Figs. 5(a) and 5(b) show oscillations of overestimating and underestimating the dose as one proceeds outward from the central beam. Such patterns are present in all of the GBFP results to some degree, but these effects are dampened as the mean free path is shortened and as one goes further from the source. In the random hinge results, the material boundary crossing error appears to be the primary source of error. In the ITS-like results, the dose is overestimated along the central beam and underestimated along the fringes of the beam. This appears to be caused by the algorithm not allowing angular deflection until the end of the electron step. Dose is deposited deeper into the geometry, and backscattering is underestimated.

5 EFFICIENCY

The accuracy of each of the approximate methods can be varied by a single parameter in the scattering kernel. For the condensed history methods, the step length can be varied. For the hybrid discrete and hybrid exponential kernels, the mean free path of the smooth screened Rutherford component can be varied. For the discrete scattering-angle kernel, the number of discrete angles can be varied (although, unlike the other kernels, this does not vary continuously). However, the runtime of each method increases as the accuracy is improved. The efficiency of the methods can only be examined by evaluating the accuracy of the method versus the computational expense.

For the geometry discussed in Section 4, the efficiency is evaluated in Figs. 6 and 7 for the line source and pencil beam problems, respectively. Here we have chosen to measure accuracy as an L2-norm of the relative error fraction over the entire problem geometry. There are two limiting factors in these studies. The first is that there is a computational expense for tracking electrons through the geometry, applying the CSD approximation, and recording energy deposition, which limit the speed of the fastest calculations. The second is that there is statistical uncertainty in the analog benchmark results, which limits the assessment of the accuracy of the most accurate calculations. In Fig. 6, we observe that the uncertainty of 0.003 in the L2-norm has caused the accuracy of the methods to asymptotically approach that value. In Fig. 7, the accuracy of the methods are approaching the limits of the statistical uncertainty at 0.015. (Because the analog calculations are much slower than the approximate methods, fewer histories were run to obtain the analog benchmarks, and they have greater statistical uncertainty.)

By the measures presented here, the hybrid discrete kernel generally looks most appealing, and the ITS-like method generally looks least appealing. There are a number of cautions that must be applied to these conclusions. The error in the random hinge results is mostly due to material boundary crossings. Presumably, a more accurate boundary crossing algorithm could improve the efficiency of the random hinge method. However, since the boundary crossing algorithm is certain to add some expense and the GBFP methods show little loss of accuracy due to boundary crossings, examining problems with many material boundary crossings may still

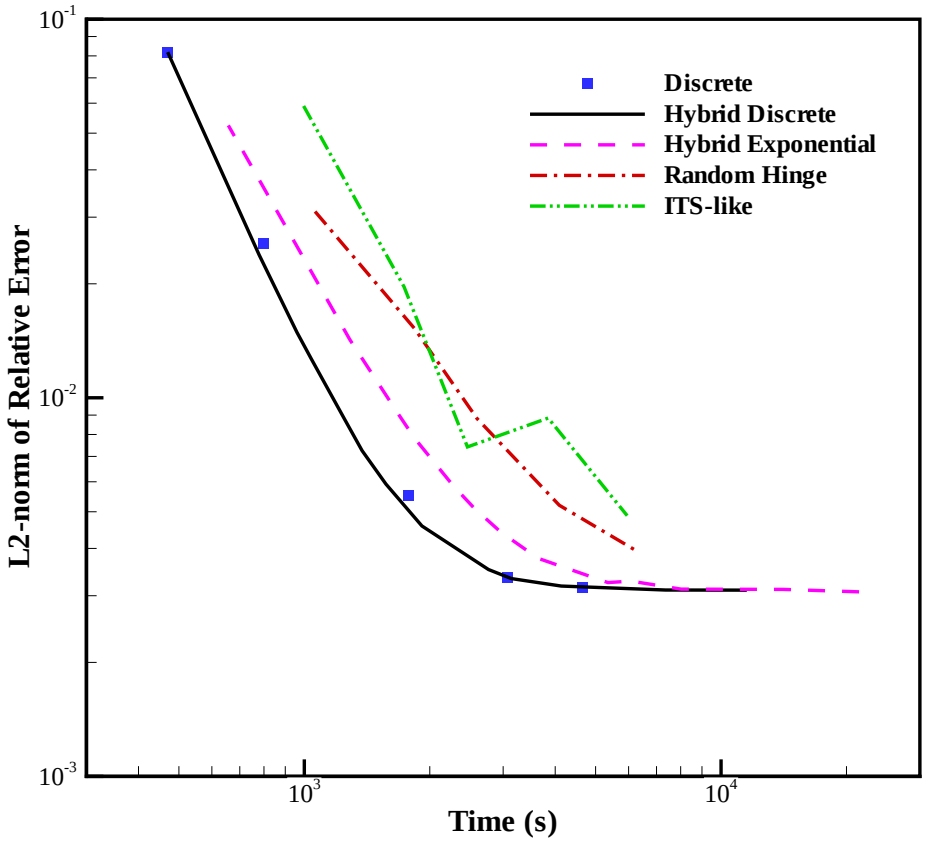

Figure 6: L2-norm of the relative error of approximate electron transport methods for a monodirectional line source.

favor the GBFP methods.

6 CONCLUSIONS

The GBFP methods offer computational effi ciency comparable to the widely-used random hinge condensed history method. Unlike condensed history methods, the GBFP methods remain accurate and retain algorithmic simplicity in the presence of material boundary crossings. Their accuracy is limited by overestimation of the uncollided (and few-collided) flux at shallow depths. However, this effect can be readily controlled by increasing the number of moments preserved or by shortening the smooth component mean free path. Of the strategies examined here, the “hybrid discrete” is the most effi cient.

7 ACKNOWLEDGMENTS

Sandia is a multiprogram laboratory operated by Sandia Corporation, a Lockheed Martin Company, for the United States Department of Energy’s National Nuclear Security Administration under Contract DE-AC04-94AL85000. The work of the second author (AKP) was

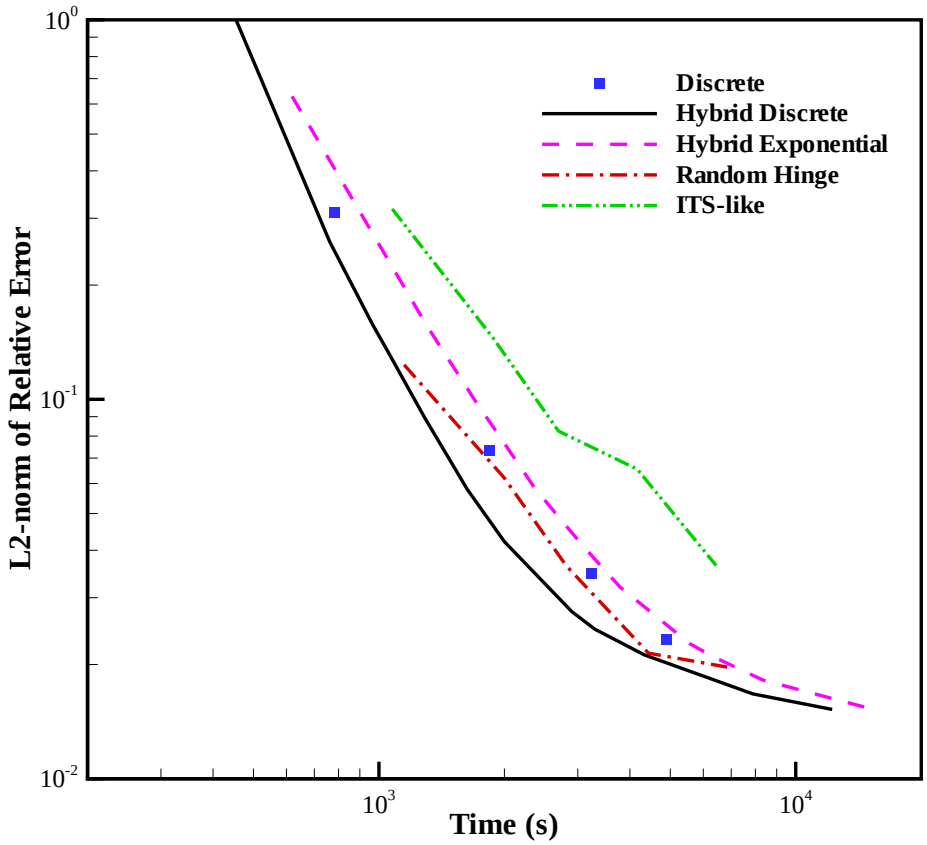

Figure 7: L2-norm of the relative error of approximate electron transport methods for a pencil beam source.

supported in part by a grant from the Department of Energy under the award DE-FG07-02ID14336.

8 REFERENCES

1. M. J. Berger, "Monte Carlo Calculations of the Penetration and Diffusion of Fast Charged Particles," in *Methods in Computational Physics*, Vol. 1, edited by B. Adler, S. Fernbach and M. Rotenberg, Academic Press, New York (1963).
2. E. W. Larsen, "A Theoretical Derivation of the Condensed History Algorithm," *Ann. Nucl. Energy*, **19**, p. 701 (1992).
3. I. Kawrakow and A. F. Bielajew, "On the Condensed History Technique for Electron Transport," *Nucl. Instr. Methods*, **B 142**, p. 253 (1998).
4. D. R. Tolar and E. W. Larsen, "A Transport Condensed History Algorithm for Electron Monte Carlo Simulations," *Nucl. Sci. Eng.*, **139**, p. 47 (2001).
5. G. C. Pomraning, "Higher Order Fokker-Planck Operators," *Nucl. Sci. Eng.*, **124**, p. 390 (1996).

6. A. K. Prinja and G. C. Pomraning, “A Generalized Fokker-Planck Model for Transport of Collimated Beams,” *Nucl. Sci. Eng.*, **137**, p. 227 (2001).
7. C. L. Leakeas and E. W. Larsen, “Generalized Fokker-Planck Approximations of Particle Transport with Highly Forward-Peaked Scattering,” *Nucl. Sci. Eng.*, **137**, p. 236 (2001).
8. A. K. Prinja and L. T. Harding, “An Energy-Loss Decomposition Scheme for Effi cient Energy Straggling Computations,” *Trans. Am. Nucl. Soc.*, **89**, p. 503 (2003).
9. B. C. Franke and A. K. Prinja, “Monte Carlo Electron Dose Calculations Using Discrete Scattering Angles and Discrete Energy Losses,” *Nucl. Sci. Eng.*, **149**, p. 1 (2005).
10. H. W. Lewis, “Multiple Scattering in an Infi nite Medium,” *Phys. Rev.* **78**, p. 526 (1950).
11. B. C. Franke and A. K. Prinja, “Discrete Scattering-Angle Model for Electron Pencil Beam Transport,” *Trans. Am. Nucl. Soc.*, **86**, p. 206 (2002).
12. B. C. Franke and A. K. Prinja, “Ray Effect Mitigation for Electron Transport with Discrete Scattering Angles,” *Trans. Am. Nucl. Soc.*, **87**, p. 133 (2002).
13. A. K. Prinja and B. C. Franke, “A Regularized Boltzmann Collision Operator for Highly Forward Peaked Scattering,” *Trans. Am. Nucl. Soc.*, **90**, p. 281 (2004).
14. D. P. Sloan, “A New Multigroup Monte Carlo Scattering Algorithm for Neutral and Charged-Particle Boltzmann and Fokker-Planck Calculations,” Technical Report SAND83-7094, Sandia National Laboratories (1983).
15. E. A. Straker et al., “MORSE Code: A Multigroup Neutron and Gamma-Ray Monte Carlo Transport Code,” Technical Report ORNL-4716, Oak Ridge National Laboratory (1970).
16. J. E. Morel, L. J. Lorence, R. P. Kensek, J. A. Halbleib and D. P. Sloan, “A Hybrid Multigroup/Continuous-Energy Monte Carlo Method for Solving the Boltzmann-Fokker-Planck Equation,” *Nucl. Sci. Eng.*, **124**, p. 369 (1996).
17. R. Evans, *The Atomic Nucleus*, McGraw-Hill, Inc., New York (1976).
18. L. L. Carter and C. A. Forest, “Transfer Matrix Treatments for Multigroup Monte Carlo Calculations – The Elimination of Ray Effects,” *Nucl. Sci. Eng.*, **59**, p. 27 (1976).
19. L. Mao, J. P. Both and J. C. Nimal, “Transfer Matrix Treatments in TRIMARAN-II, Nonequally Probable Step Function Representation in Multigroup Monte Carlo,” *Nucl. Sci. Eng.*, **130**, p. 226 (1998).
20. J. A. Halbleib, R. P. Kensek, T. A. Mehlhorn, G. D. Valdez, S. M. Seltzer and M. J. Berger, “ITS Version 3.0: The Integrated TIGER Series of Coupled Electron/Photon Monte Carlo Transport Codes,” Technical Report SAND91-1634, Sandia National Laboratories (1992).
21. D. C. Jensen, “Monte Carlo Calculation of Electron Multiple Scattering in Thin Foils,” Master’s Thesis, Naval Postgraduate School, Monterey, California (1988).